Biological sciences

Biophysics and Computational Biology

Live-cell super-resolution microscopy reveals a primary role for diffusion in polyglutamine aggresome assembly

Short title: mechanistic process of aggresome formation

Meng Lu[a], Luca Banetta[b,1], Laurence J. Young[a,1,†], Edward J. Smith[c], Gillian P. Bates[c], Alessio Zaccone[b], Gabriele S. Kaminski[a], Alan Tunnacliffe[a], Clemens F. Kaminski[a,2]

[a]Cambridge Infinitus Research Center, Department of Chemical Engineering and Biotechnology, University of Cambridge, Cambridge, CB3 0AS, United Kingdom

[b]Department of Chemical Engineering and Biotechnology, University of Cambridge, Cambridge, CB3 0AS, United Kingdom

[c]Sobell Department of Motor Neuroscience and Movement Disorders and Huntington's Disease Center, Institute of Neurology, University College London, London, WC1N 3BG, United Kingdom

[†]Current address: Fluidic Analytics, Unit 5, Chesterton Mill, French's Road, Cambridge, CB4 3NP, United Kingdom

[1]L.B. and L.Y. contributed equally to this work.

[2]To whom correspondence should be addressed. Department of Chemical Engineering and Biotechnology, University of Cambridge, Cambridge, CB2 3RA, United Kingdom. Email: cfk23@cam.ac.uk (C. F. K.), Tel: +44(0) 1223 763135

Keywords: live cell SIM, dynamics of aggregate, aggresome formation, active transport, passive transport

Abstract

The mechanisms leading to self-assembly of misfolded proteins into amyloid aggregates have been studied extensively in the test tube under well controlled conditions. However, to what extent these processes are representative of those in the cellular environment remains unclear. Using super-resolution imaging of live cells, we show that an amyloidogenic polyglutamine-containing protein first forms small, amorphous aggregate clusters in the cytosol, chiefly by diffusion. The dynamic interaction among these clusters limits their elongation and leads to structures with a branched morphology, which differ from the predominantly linear fibrils observed *in vitro*. A proportion of these clusters then assemble via active transport at the microtubule organising center to initiate the formation of perinuclear aggresomes. Although it is widely believed that aggresome formation is entirely governed by active transport along microtubules, we demonstrate, using a combined approach of advanced imaging and mathematical modeling, that diffusion becomes the principal mechanism driving aggresome expansion. The increasing surface area of the expanding aggresome increases the rate of accretion due to diffusion of cytosolic aggregates, and this pathway soon dominates the aggresome assembly process. In extreme cases, this is sufficient to clear the cytoplasm of peripheral clusters. We also show that aggresomes mature over time, becoming more compacted as the structure grows. The presence of large perinuclear aggregates profoundly affects the behaviour and health of the cell and here we show via super-resolution imaging that aggresome formation and development are governed by highly dynamic processes that are important in the design of potential therapeutic strategies. (250 words)

Significance statement

Aggresome formation, which leads to severe cell damage including DNA breaks and apoptosis, is believed to be solely governed by active transport of protein aggregates along microtubules. However, we have used super-resolution imaging and mathematical modeling to show that diffusion, in fact, is the predominant process in aggresome assembly. Diffusion of aggregation-prone proteins initially drives formation of small, branched aggregate clusters, which undergo random motion and demonstrate fast fusion and fragmentation behaviour. Active transport along microtubules is then responsible for aggresome nucleation, but diffusion plays the main role in further deposition of aggregate clusters, which occurs at an increasing rate as the aggresome expands. Our data also highlight the marked contrast between in-cell and *in vitro* aggregate assembly processes. (120 words)

“\body”Introduction

The misfolding of polypeptides and their subsequent aggregation into insoluble amyloids is a characteristic of many neurodegenerative diseases (1, 2). Polyglutamine (polyQ) is generated by the expansion of clustered glutamine codons in various unrelated protein-coding genes and is implicated in neurodegenerative conditions such as Huntington’s disease (HD). Accumulation of misfolded polyQ leads to the formation of aggregates in cytosol and aggresomes near the microtubule organising center (MTOC) (3), but the details of the protein aggregation process remain unclear. In a previous study (4), we showed that cells first generate cytoplasmic aggregates which coalesce into aggresomes, which take up a considerable volume in the cell and can lead to DNA damage and interference with the cell cycle (5, 6). Mechanistic information on the assembly process of misfolded proteins is clearly of pathological significance, and investigations at the molecular scale are critical to a detailed understanding of this process. Conventionally, the kinetics of amyloid aggregation reactions are studied in the test tube. *In vitro* experiments have for example demonstrated how monomers of polyQ proteins assemble at seeding sites, leading to elongation of fibrillary aggregates (7, 8). Such fibrils grow to 1-2 μm in length *in vitro*, and they feature a well-defined morphology and are subsequently bound into loosely compacted bundles (9, 10).

In vitro experiments enable perfectly adjusted solution conditions, where protein nucleation, diffusion and elongation kinetics can be tightly controlled (11). However, the intracellular environment is far more complex, featuring active transport, multiple phases, molecular crowding, and compartmentalisation, all of which likely affect the kinetics and attributes of protein aggregate formation (12). Therefore, although *in vitro* assays are a convenient tool, their relevance to the physiological situation needs to be examined. In cells, polyQ aggregates appear to be structurally heterogeneous, being composed of a mixture of granules, straight and tortuous filaments, and fibrils (13). Intriguingly, fibrillar structures in cells are typically 7-8 nm in diameter, similar to their *in vitro* counterparts, but their length rarely exceeds 300 nm or so (14). They are thus morphologically similar to those formed *in vitro* but of significantly reduced length (10). In terms of dynamics, intracellular aggregates display distinct patterns that differ fundamentally from their in-solution counterparts. A previous study has demonstrated the remarkable mobility of polyQ aggregates within the cell nucleus and these intranuclear aggregates were shown to disrupt normal patterns of gene expression (15). In the current paper we focus on the formation of aggresomes in the cytosol. We investigate the nucleation and expansion phases of aggresomes in the perinuclear region and distinguish active from passive

transport phenomena. Using a combination of advanced optical imaging modalities, including high speed structured illumination microscopy (SIM), single particle tracking (SPT), and mathematical modeling of aggregate transport in the cell, we establish that aggresome formation is initiated by active transport of small aggregates, which are dispersed throughout the cytosol, to the MTOC. However, at later stages aggresome expansion is mainly driven by diffusion of protein aggregates.

Results

Aggresomes expand in volume by recruitment of polyQ clusters

We have previously established stable HEK cell lines expressing a tetracycline-inducible partial exon 1 sequence of huntingtin protein with an expanded polyQ region of 72 glutamine residues (HDQ72) fused to the SNAP-tag protein or to EGFP (6). With continuous induction of HDQ72, intracellular polyQ aggregates, including perinuclear aggresomes, begin to appear within a week (Fig. 1*A*, Fig. S1*A*), although the proportion of the cell population containing aggregates remains more or less constant at about 30 percent (Fig. S1*B*). This suggests that any aggregate-containing cells that die are replaced by newly divided cells, in which aggregation is already underway, or is imminent (6).

To assess aggregate formation in real time, we performed time-lapse imaging of cells expressing EGFP-HDQ72, with image capture every 15 min over a 15 h period (Fig. 1*A* and *B*). We observed the appearance and gradual increase in size of a compact perinuclear aggresome (white arrows in Fig. 1*A*), while the fluorescence of the rest of the cytoplasm simultaneously decreased (Fig. 1*A* and *C*). In contrast, the fluorescence intensity in cells without aggregates remained constant throughout this time period (Fig. 1*B* and *C*). Quantification of cytoplasmic fluorescence intensity, excluding the main aggregation site, revealed lower fluorescence intensity in aggregate-containing cells in comparison to non-aggregate containing cells (Fig. 1*D* upper panel). Furthermore, plotting the average cytoplasmic fluorescence against the size of aggregates showed these parameters to be inversely correlated with each other (Fig. 1*D* lower panel). Taken together, these findings suggest that large polyQ aggresomes are formed in the perinuclear region, presumably by continual accretion of monomers or small aggregates from the cytosol. In addition, even when polyQ protein is continuously expressed, a large aggresome seems able to clear the cytoplasm of the majority of smaller aggregates.

Aggregate assembly in cells is determined by an interplay of diffusion and active transport processes

The growth of perinuclear aggresomes at the expense of the cytosolic polyQ fraction led us to investigate how monomeric HDQ72 or small aggregates are added to the perinuclear site. To address this, we performed high-resolution spatio-temporal imaging of aggregation events by SIM (16) using a custom-built setup, capable of 90 nm spatial resolution at frame rates of up to 22 Hz (17). The resulting time-lapse videos revealed that cytosolic polyQ aggregates are small compact structures, which are clusters of short fibrils and highly branched and labile in nature, frequently undergoing rapid motion (Video 1), with a size that rarely exceeds ca. 500 nm in scale (Fig. 2). Therefore, we define these small aggregated species as aggregate clusters. Using a SPT algorithm, we identified individual aggregate clusters and analysed their trajectories over a 24 s period at a frame rate of 5 Hz (Fig. 2*A*). The data revealed motion that is overwhelmingly random in fashion for most of the clusters identified. Individual particles moved at speeds ranging from 0 to 2 μm s^{-1} and were initially in localized domains where they fused with other clusters, as shown in Fig. 2*B* and Video 2. In addition to random movement, a small proportion of aggregates appeared to be transported actively, as indicated by rapid linear movements over distances up to 8 μm. In total, less than 3% of all aggregates were found to undergo active transport. Fig. 2*C* shows both passive (diffusional) and active transport events for small clusters. The zoomed regions show that passive transport can lead to both the fission (fragmentation) of aggregate clusters (red rectangle) and their fusion (orange rectangle). The former is suggestive of shear forces prevailing in the dense and multiphasic cellular environment. Unlike the situation *in vitro*, the size of the elongated aggregates within cells appears to be limited by fragmentation: only 1% of clusters were observed to extend beyond 1.5 μm in size, and 90% of all clusters were less than 500 nm in size (Fig. S2). The fusion revealed that small aggregates cluster by fusion of different aggregate particles (orange rectangles in Fig. 2*B* and *C*). Even within large aggresomes, individual small clusters were in motion (Fig. 2*D* and Video3), although at slower speeds than their freely diffusing counterparts (Fig. 2*B* and *C*). There is also evidence of active transport in Fig. 2*C*: along the green track shown in the left panel, one observes highly directed motion, likely along a microtubule (MT).

It was previously suggested that small aggregates are transported along MTs to form aggresomes at the MTOC, as MT inhibition via nocodazole treatment resulted in a pronounced reduction in the formation of aggresomes (3, 18, 19). Our data provide strong and direct evidence of aggregate transport along directional tracks, likely along MTs. We measured active transport at velocities averaging around 1 μm s^{-1}, which is of the order expected for microtubule-assisted transport by motor proteins (20, 21). Although active transport represents only a very small proportion of cluster movements, over

long periods of time (>16 h) most cytosolic clusters had translocated to a perinuclear region near the MTOC. The most parsimonious explanation of this observation is that diffusion is responsible for this deposition of aggregated polyQ protein at the aggresome. Indeed, as shown below, this is likely to be the predominant mechanism, because, as shown in Figure 1*A*, almost all of the cytosolic polyQ is adsorbed onto the aggresomes after 16 h. In summary, our recordings reveal a highly dynamic interplay between fragmentation and fusion, and between diffusional and active transport, all of which affect the formation and fate of small aggregate clusters within cells.

A small proportion of aggregate clusters bind with HDAC6 and MTs

Previous studies reported that cytosolic aggregates are recruited by HDAC6 and bind to dynein for active transport along MTs (22, 23). Therefore, to gain further information on the degree of active transport of polyQ clusters in our model, we performed immunostaining against HDAC6 and tubulins in HDQ72-expressing cells, followed by super-resolution imaging and 3D reconstruction. In Fig. 3*A*, 3D rendering of the zoomed-in region shows dense distributions of aggregate clusters (green) and HDAC6 (red); however, aggregate clusters recruited by HDAC6, which display overlapped regions in yellow (Fig. 3*A*, right panel), are not widely observed. We quantified the proportion of clusters recruited by HDAC6 and found that they represent ca. 11% of all aggregates. In Fig. 3*B*, super-resolved structures of MTs (red) and aggregate clusters (green) demonstrate similar results, showing that ca. 9% of aggregates are attached to tubulins (highlighted by blue arrows in the right panel). These numbers are higher than the fraction of aggregate clusters that were observed to undergo directional transport (3%, see earlier section). The difference may suggest that some MT associated transport appears random in motion as reported in (24) may thus not have been discriminated in the motion analysis of the SPT tracks.

Large perinuclear aggresomes comprise adsorbed amorphous polyQ clusters that arrive from the cytosol

Super-resolution microscopy offers morphological and structural details of large perinuclear aggresomes. Fig. 4 shows a perinuclear aggresome, imaged with 3D SIM (Fig 4*A*, and Video 4), which reveals amorphous structures near the aggresome core, with small, isolated clusters appearing in the periphery (Fig. 4*A*, zoomed in region of 1 and 2 and Video 5). The small polyQ aggregate clusters feature a very different morphology to those observed in the test tube, e.g. in fibril elongation assays (25, 26), or the fibril bundles formed in solution (27), both of which feature clearly defined linear structures. Instead, the cytosolic clusters we observe here, have multiple, tangled branches and are limited in size to less than 1.5 μm. The appearance of a dense core region of the aggresome and a less

compacted peripheral region containing discernible individual species led us to speculate that individual small clusters are recruited to the large perinuclear aggresomes located at the MTOC (3), and that this association and the ensuing aggresome growth and compaction are responsible for the consumption of cytoplasmic protein material presented in Fig. 1.

Aggresomes are assembled by small clusters in an irreversible and partially disordered fashion by diffusion, which leads to their amorphous and tangled morphology. Assembly of amorphous aggregates in this fashion has been shown to lead to structures with fractal morphologies (28). To test whether this premise is true in the present case, and to give further credence to the hypothesis that aggresome development is primarily governed by diffusion driven phenomena we performed a fractal analysis on the evolving aggresome topologies. We calculated the fractal dimension D_f, relating the cluster mass to the evolving cluster sizes (see *Materials and Methods* and Fig. S3). The results show that the radius of gyration (used as a characteristic measure of cluster size) scales linearly with the number of small clusters identified within them, an observation typical of fractal objects (Fig. 4*B*). In what follows, the fractal dimension is used in a computational model of aggresome formation.

Mathematical modeling of aggresome formation and expansion

To gain a better understanding of our experimental observations, we developed a mathematical model describing the formation and growth of perinuclear aggresomes, which included both diffusion and active transport processes. We considered an aggresome to be a spherical fractal ensemble of elementary building blocks, resembling the experimental observation of cytosolic clusters assembling into a fractal superstructure. Transport was modelled using a diffusion equation to mimic Brownian motion of aggregate clusters in the cytosol and a pure advection equation for active transport to the MTOC along MTs. The model reduces to a moving-boundary transport problem where two distinct motion processes take place at the same time. This leads to two Cauchy problems, linked by overall matter conservation, for diffusion and active transport, respectively, in a spherical geometry. Conservation of matter at the solid-liquid (or aggresome surface) interface is implemented to describe the quantity of polyQ clusters migrating into the growing aggresome and to update the position of the radius of the expanding aggresome (the moving lower boundary of the domain where the differential equations are solved). Full details of the computational approach are presented in the Supporting Information.

Fig. 5*A* compares the experimentally measured growth of aggresomes over a 16-hour span with the model results. The full model (black line) comprises both active transport (green line) and diffusion (blue line) components and provides an excellent fit to the experimental data (red dots). The model clearly demonstrates that aggresome growth is dominated by diffusion, although inclusion of active transport is required in a comprehensive model of the process. Next, we correlated the aggresome expansion in time with the concentration of aggregate clusters in the cytosol (Fig. 5*B*). As time increases (colour of curves changing from black to red), the cytosolic concentration is clearly seen to decrease (decrease in plateau region of curves, at far distance). For each time point, the cytosolic concentration is also seen to decrease with proximity to the aggresome surface, thus the process exhibits clear source-sink behaviour. The trends captured in the model shown in Fig. 5*B*, are consistent with the results from the time-lapse imaging shown in Fig. 1*A*, which also shows a continuously decreasing cytosolic of polyQ concentration as aggresome grow in size. Recruitment of clusters leads to aggresome expansion and depletion of cytosolic clusters. It is interesting to note, that in some cells, the cytosolic polyQ concentration was not observed to change in time, and no substantial aggresomes formed (Fig. 1*B*). This observation, in conjunction with the modelling results, suggests that there exists a delicate balance of cluster formation and removal rates in the cell, which will be discussed in further detail in the following sections.

The aggresome core becomes increasingly dense over time

To further validate our observation and modeling that perinuclear aggresomes grow by accretion of cytoplasmic material, we devised an experimental system to visualize the addition of newly synthesised polyQ protein onto existing perinuclear aggresomes using a stable cell line for inducible expression of SNAP-tagged HDQ72 protein (5). In this system, newly synthesised protein of interest can be irreversibly, covalently and sequentially labelled by two different dyes (29). Thus, we induced the expression of SNAP-HDQ72 with tetracycline for 14 days to allow aggregates to form and then added TMR-Star (580 nm emission peak, red) to the culture for 30 min to label the HDQ72 protein already synthesised within the cells. We then replaced the medium containing TMR-Star and grew the cells for three more days without label before adding 505-Star (532 nm emission, green) for 30 min. This allowed newly expressed HDQ72 protein to be labelled with a different colour. After washing out 505-Star, cells were incubated at 37˚C for another two hours to stabilise them before fixation with ice cold methanol followed by confocal microscopy (Fig. 6*A*).

We identified two types of aggresome in this way. First, aggresomes were observed in which the core was labelled by both colours, suggesting that the newly expressed HDQ72 could enter the core region of an already formed aggresome (agg1 in Fig. 6*A*). Second, we observed aggresomes with a red core surrounded by a green shell of newly added HDQ72, indicating that such aggresomes have an impermeable core (agg2 in Fig. 6*A*). A typical aggresome of this type is also shown in a series of confocal z-stack images to provide a 3-D overview (Fig. 6*A*, right-most panel). High resolution SIM imaging (Fig. 6*B*) revealed some mixing of SNAP labels at the interface between core (red) and peripheral shell (green), consistent with the surface of such aggresomes being less compact than the core, permitting diffusive mixing and intercalation of fragments on the aggresome surface.

We were able to demonstrate, using the labelling scheme in Fig. 6*A* and a series of confocal z-stack images, that, while large aggresomes consist of proteins expressed during both labelling periods (Fig. 6*C*, white arrows), small aggregates (Fig. 6*C*, red arrows) separate from this aggresome were composed only of newly expressed proteins (green only). This indicates that small aggregate clusters are either transported to aggresomes, or that they are degraded within a few days of synthesis. This directly confirmed our modeling that aggresomes initiate from a nucleation site and then expand rapidly by attracting small aggregate clusters. We also found that aggresomes with an impermeable core comprise less than 20% of the total population after three month of gene induction. Compared with permeable aggresomes that vary in size from 1 μm to 9 μm in diameter, impermeable aggresomes are all >4 μm in diameter, indicating that an impermeable core structure is associated with larger aggresomes. In summary, our two-colour labelling experiments suggest that aggresomes mature from permeable, loose structures into structures with more compacted cores (Fig. 6*D*). We take two potential conclusions from the observations presented so far. First, aggregated protein in late-stage aggresomes with compacted cores is less likely to dissociate. Second, the increasing surface area of late aggresomes increases the probability that new material will adsorb. Taken together, these phenomena may explain the near-complete depletion of cytosolic polyQ in cells where large aggresomes are present (see Fig. 1*A*). It may also explain why in some cells large aggresomes never form, because in these cases fragmentation is dominant over accumulation. These processes are distinctly different to what is observed in test tube experiments.

The morphology of polyQ aggregates in cell models mimics that of aggregates in a mouse model of Huntington's disease

One of the characteristics of HD is the accumulation of polyQ aggregates in both nuclear and cytoplasmic regions of brain cells. To investigate to what extent our data reflect the morphological details of polyQ structures found in models of HD pathology, we performed experiments in brain sections of the R6/2 mouse, a transgenic strain that expresses a version of exon1 of the human huntingtin gene that encodes at least 150 glutamine repeats (30). Fig. 7*A* shows a large nuclear aggregate visualised with 3D SIM using the EGFP-HDQ72 HEK cell model. The structure is similar in appearance to that of perinuclear aggresomes in that cell model (see Fig. 4), although the mechanisms of formation are likely different in the nucleus. The brain sections from the R6/2 mouse were immunostained with the S830 anti-huntingtin antibody and imaged for comparison. In contrast to the HEK cell model, perinuclear aggresomes were less abundant and large aggregates featured predominantly in the nuclear domain. However, the morphology of nuclear aggregates appeared very similar to that in the HEK cell model (see Fig. 7*B*). Again, the aggregates appear highly condensed at their core (white arrow, Fig. 7*A* and *B*), but more loosely structured at their periphery.

The experiments confirmed that the morphological diversity of aggregate structures formed in the mouse model is similar to that in the HEK cell model, confirming that the cell line is representative of protein aggregation in models of HD, thus providing a convenient means to study molecular aspects of the disease and therapeutic strategies.

Discussion

PolyQ fibril formation kinetics have been widely studied both *in vitro* under controlled solution conditions. However, polyQ aggregates formed in cells show different structural characteristics to their *in vitro* counterparts. For example, elongation into long fibrillary structures has not been observed in the cell, and fibrils do not usually extend significantly beyond a mean length of ca. 125 nm (14), in stark contrast to their solution counterparts, which can extend to several microns in length (9, 10). Our experiments demonstrate that the assembly of short fibrils into larger structures is primarily driven by diffusion rather than elongation by end-on monomer addition, but also involved fast fusion and fragmentation events that lead to the formation of branched clusters of ca. 500-1000 nm in diameter.

This, together with other data we report here, leads to a different view of aggresome formation than proposed previously. It has been suggested that aggresome formation is dependent on HDAC6- and dynein-facilitated active transport along MTs (22). While we find that this is an important first step in the nucleation of aggresomes, subsequent aggresome expansion is primarily driven by diffusion. A

model of aggresome formation shows that, initially, rates of aggregate accumulation via active transport and diffusion are comparable (Fig. 5*A*), but they rapidly diverge once nucleation has occurred (time 0 in Fig. 5*A*). The nascent aggresome near the MTOC grows in size and forms amorphous and fractal objects (Fig. 4*B*) with rapidly increasing surface area (Fig. 1*A* and 5*B*). This accelerates the capture rate for new aggregate material arriving by diffusion (Fig. 5*B*) and this gradually becomes the primary route for aggresome expansion (Fig. 5*A* and *C*). The model explains why in some cells the soluble and cytosolic fraction of polyQ gets rapidly depleted, because the rate of consumption by the aggresome exceeds the production of new protein (see Fig.1*A* and 5*B* for experimental and model data, respectively). On the other hand, some cells do not form aggresomes at all, and the initial nucleation near the MTOC never takes place. This suggests that in these cells degradation mechanisms, e.g. by lysosomal or UPS mediated degradation of monomeric species, are sufficiently strong to prevent the formation of cytosolic aggregate clusters and this prevents their subsequent assembly into aggresomes. On the other hand, our study shows that transport of small fibrils from the cytosol, leads to the nucleation of aggresomes near the MTOC. Strategies for therapeutic intervention should thus focus on preventing the nucleation of small aggregate species in the cytosol, keeping the protein pool soluble in order for UPS degradation to function optimally, and thus preventing fibrillary species from arriving at the MTOC. Fibrillar structures are known to be difficult to degrade in the cell (31, 32) and thus their transport to the MTOC just leads to irreversible clustering. This suggests that the UPS that can target monomers for degradation (32, 33, 34) is a key target for the prevention of aggresome formation. The conclusions are consistent with a previous finding that inhibition of the active transport pathway via nocodazole treatment of cells, known to lead to microtubule depolymerisation, did indeed prevent aggresome formation near the MTOC, however, it led to protein accumulation and aggregation in the cytosol (3; 18, 19).

In the literature, there is an ongoing debate on the relative toxicities of monomeric and aggregated protein species in the cell (35). Much of the recent literature has focused on soluble species as the main problem in amyloid mediated neuropathology and suggestions have been made to drive the amyloidogenic protein species into an aggregated and thus more passive state (36, 37). However, the current work suggests that this may not be the right strategy after all: Large intracellular aggregates have been shown to produce long term toxicity, for example, by inducing DNA damage and apoptosis (6). Therefore, increasing the rate of fibril formation in the cytosol may be a risky strategy, as this enhances the likelihood of aggresome formation as we show here.

In conclusion, we have shown through a combined approach of advanced experimental analysis and modelling that both ATP mediated and purely passive, physical phenomena play very important roles in the homeostasis of misfolded protein. The study highlights differences as well as similarities of the protein aggregation processes occurring *in vitro* and in the cell.

Materials and Methods

Materials

L-glutamine, zeocin, hygromycin, blasticidin, DMEM, PBS, FBS, hoechst33342 solution and agarose were purchased from Sigma-Aldrich. TMR-Star and 505-Star staining reagents were purchased from New England Biolabs. Antibodies against HDAC6 (7558S) (dilution for immunofluorescence 1:300) were from Cell Signalling Technology, and against α -tubulin (T5168) (dilution for immunofluorescence 1:300) from Sigma-Aldrich.

Cells

Details on plasmids and construction of the stable cell line were as described previously (Lu et al., 2015 B). Briefly, mammalian Flp-In T-REx293 cells were grown in T75 or T25 flasks or 6-well plates by incubation at 37°C in a 5% CO_2 atmosphere. Complete medium for normal cell growth consisted of 90% DMEM, 10% FBS with 2 mM L-glutamine; antibiotics were used as appropriate. Cells were kept in logarithmic phase growth and passaged on reaching 80-90% confluence (approximately every 3-4 days). Medium was changed every two or three days.

Mice

All experimental procedures performed on mice were conducted under a project licence from the Home Office (Animal Scientific Procedures Act 1996) and approved by the King's College London Ethical Review Process Committee. Hemizygous R6/2 mice (30) were bred by backcrossing R6/2 males to (CBA × C57BL/6) F1 females (B6CBAF1/OlaHsd; Harlan Olac). Mice were genotyped and the CAG repeat was measured as previously described (38). Animals were housed under a 12 h light/12 h dark cycle, with unlimited access to water and food (Special Diet Service, Witham, UK) in a conventional unit. Cages were environmentally enriched with a cardboard tube. Animals were sacrificed through terminal anesthesia with Euthatal (Marial, Harlow, UK) at 14 weeks of age. Brains were removed and fixed in 4% Parafix (Pioneer Research Chemical Ltd., Essex, UK) for 48 h. The brains were then rinsed in phosphate buffered saline (PBS) and stored in 30% sucrose, 0.05% sodium

azide in PBS until sectioning. Coronal sections from a female mouse (CAG = 215) and wild type control were taken serially at 50 μm thickness on a freezing microtome (HM430 Microm, Thermo Scientific), and stored at -20°C in tissue cryoprotective solution containing 0.05% sodium azide until staining.

Sections were washed in PBS prior to non-specific binding blocking with 1 h incubation in 10% normal serum with 0.3% Triton X- 100 in PBS. They were then incubated overnight at 4°C in primary antibody against S830 (1:2000), raised against exon 1 huntingtin with 53 glutamines (39), prior to incubation in secondary Alexa-488 fluorescent dye (Molecular Probes) for 2 h at RT. After a subsequent 15-min incubation in Hoechst (Invitrogen) sections were washed in PBS and cover-slipped with Vectashield (Vector Laboratories, Peterborough, UK).

Microscopy

After induction for various times, SNAP-HDQ72-expressing cells were incubated for 30 min at 37°C with 300 mM SNAP-Cell TMR-Star (New England Biolabs) dissolved in complete medium. After labeling, samples were washed three times with complete medium and incubated for 30 min prior to imaging. Images were recorded with an OMX V3 super-resolution microscope. Confocal microscopy and immunofluorescence protocols were as described previously (6).

Fixed samples were imaged on a confocal microscope (Leica TCS SP5, using the Leica Application Suite (LAS AF)) with a HCX PL APO 40x/1.25-0.75 oil objective lens (Leica) or HCX PL APO 60x/1.40-0.60 oil objective lens (Leica) at room temperature. Fluorochromes used for individual experiments are stated in the figure legends. For the time-lapse fluorescence intensity measurements, cells were grown in glass-bottom petri-dishes at 37°C in a 5% CO_2 atmosphere. On the day of imaging, samples were first stabilised in the incubation chamber of the Leica TCS SP5 system with continuous air supply (37°C and 5% CO_2). Complete medium was used for live-cell imaging experiments and half the medium replaced every two days. The time interval between consecutive image captures varied from 5 min to 15 min, as appropriate. The entire set-up was controlled using the Leica LAS AF software, and ImageJ was used for image processing and analysis.

For the aggresome permeability measurements, we recorded confocal image stacks for both labels used, and only those aggregates were classified as permeable aggregates that were homogenously labelled throughout their volume with both colours.

To visualize intracellular aggregate motion, we used our custom-built SIM providing a spatial resolution approaching 90 nm at frame rates reaching 22 Hz (17). Cells were grown in glass-bottom petri-dishes at 37°C in a 5% CO_2 atmosphere. On the day of imaging, petri-dishes were first stabilised in the incubation chamber of the SIM system with continuous air supply (37°C and 5% CO_2). Hardware control and image reconstruction were performed with software written in LabView and Matlab (16, 40). For motion analysis and visualisation ImageJ was used.

Footnotes

- [1]L.B. and L.Y. contributed equally to this work.
- [2]To whom correspondence may be addressed. Email: cfk23@cam.ac.uk
- The authors declare no conflict of interest.

Acknowledgements

We thank Dr Ajay Mishra for reading the manuscript and providing useful comments. We thank Dr Chiara Boschetti and Dr Clare Michel for discussions and helpful advice. This research was funded by Infinitus (China) Company Ltd, an Advanced Investigator Award (AdG233232) from the European Research Council to AT and by scholarships from the Cambridge Overseas Trust and the Chinese Scholarship Council to ML; CFK acknowledges support from EPSRC (EP/L015889/1 and EP/H018301/1), MRC (MR/K015850/1 and MR/K02292X/1) and Wellcome Trust (3-3249/Z/16/Z and 089703/Z/09/Z). GB is supported by the CHDI Foundation.

References

1. Ross CA, Poirier MA (2004) Protein aggregation and neurodegenerative disease. *NatMed* 10 Suppl(1078–8956):S10–S17.

2. Ciechanover A, Kwon YT (2015) Degradation of misfolded proteins in neurodegenerative diseases: therapeutic targets and strategies. *Exp Mol Med* 47(3):e147.

3. Johnston JA, Ward CL, Kopito RR (1998) Aggresomes: A cellular response to misfolded proteins. *J Cell Biol* 143(7):1883–1898.

4. Lu M, et al. (2015) Expression-level dependent perturbation of cell proteostasis and nuclear morphology by aggregation-prone polyglutamine proteins. *Biotechnology and Bioengineering* 112(9):1883–1892.

5. Giuliano P, et al. (2003) DNA damage induced by polyglutamine-expanded proteins. *Human Molecular Genetics* 12(18):2301–2309.

6. Lu M, Boschetti C, Tunnacliffe A (2015) Long term aggresome accumulation leads to DNA damage, p53-dependent Cell Cycle Arrest, and Steric Interference in Mitosis. *Journal of Biological Chemistry* 290(46):27986–28000.

7. Walters RH, Jacobson KH, Pedersen JA, Murphy RM (2012) Elongation kinetics of polyglutamine peptide fibrils: A quartz crystal microbalance with dissipation study. *Journal of Molecular Biology* 421(2–3):329–347.

8. Huynen C, et al. (2015) Influence of the protein context on the polyglutamine length-dependent elongation of amyloid fibrils. *Biochimica et Biophysica Acta - Proteins and Proteomics* 1854(3):239–248.

9. Streets AM, Sourigues Y, Kopito RR, Melki R, Quake SR (2013) Simultaneous Measurement of Amyloid Fibril Formation by Dynamic Light Scattering and Fluorescence Reveals Complex Aggregation Kinetics. *PLoS ONE* 8(1):1–10.

10. Duim WC, Jiang Y, Shen K, Frydman J, Moerner WE (2014) Super-resolution fluorescence of huntingtin reveals growth of globular species into short fibers and coexistence of distinct aggregates. *ACS Chemical Biology* 9(12):2767–2778.

11. Kaminski CF, Schierle GSK (2016) Probing amyloid protein aggregation with optical superresolution methods : from the test tube to models of disease. *Neurophotonics* 3(4):41807.

12. Pinotsi D, et al. (2016) Nanoscopic insights into seeding mechanisms and toxicity of α-synuclein species in neurons. *Proceedings of the National Academy of Sciences* 113(14):3815–3819.

13. DiFiglia M, et al. (1997) Aggregation of huntingtin in neuronal intranuclear inclusions and dystrophic neurites in brain. *Science (New York, NY)* 277(5334):1990–3.

14. Bäuerlein FJB, et al. (2017) In Situ Architecture and Cellular Interactions of PolyQ Inclusions. *Cell* 171(1):179–187.e10.

15. Li L, et al. (2016) Real-time imaging of Huntingtin aggregates diverting target search and gene transcription. *eLife* 5(AUGUST):1–29.

16. Strtohl F, Kaminski CF (2016) Frontiers in structured illumination microscopy. *Optica* 3(6):667–677.

17. Young LJ, Ströhl F, Kaminski CF (2016) A Guide to Structured Illumination TIRF Microscopy at High Speed with Multiple Colors. *Journal of visualized experiments : JoVE* (111):e53988.

18. Taylor JP, et al. (2003) Aggresomes protect cells by enhancing the degradation of toxic polyglutamine-containing protein. *Human Molecular Genetics* 12(7):749–757.

19. Wang H, Ying Z, Wang G (2012) Ataxin-3 regulates aggresome formation of copper-zinc superoxide dismutase (SOD1) by editing K63-linked polyubiquitin chains. *Journal of Biological Chemistry* 287(34):28576–28585.

20. Verhey KJ, Kaul N, Soppina V (2011) Kinesin Assembly and Movement in Cells. *Annual Review of Biophysics* 40(1):267–288.

21. Howard J (1997) Molecular motors: structural adaptations to cellular functions. *Nature* 389(6651):561–567.

22. Kawaguchi Y, et al. (2003) The deacetylase HDAC6 regulates aggresome formation and cell viability in response to misfolded protein stress. *Cell* 115(6):727–738.

23. Iwata A, Riley BE, Johnston JA, Kopito RR (2005) HDAC6 and microtubules are required for autophagic degradation of aggregated Huntingtin. *Journal of Biological Chemistry* 280(48):40282–40292.

24. Balint S, et al. (2013) Correlative live-cell and superresolution microscopy reveals cargo transport dynamics at microtubule intersections. *Proc Natl Acad Sci USA* (110):3375–3380.

25. Buchanan LE, et al. (2014) Structural motif of polyglutamine amyloid fibrils discerned with mixed-isotope infrared spectroscopy. *Proceedings of the National Academy of Sciences* 111(16):5796–5801.

26. Pinotsi D, et al. (2014) Direct observation of heterogeneous amyloid fibril growth kinetics via two-color super-resolution microscopy. *Nano Letters* 14(1):339–345.

27. Ren PH, et al. (2009) Cytoplasmic penetration and persistent infection of mammalian cells by polyglutamine aggregates. *Nature Cell Biology* 11(2):219–225.

28. Jullien R. (1987) Aggregation phenomena and fractal aggregates. *Cont. Phys.* **28**, 477–493.

29. Keppler A, et al. (2003) A general method for the covalent labeling of fusion proteins with small molecules in vivo. *Nature biotechnology* 21(1):86–9.

30. Mangiarini L, et al. (1996) Exon I of the HD gene with an expanded CAG repeat is sufficient to cause a progressive neurological phenotype in transgenic mice. *Cell* 87(3):493–506.

31. Gandy S, Heppner FL (2005) Breaking up (amyloid) is hard to do. *PLoS Medicine* 2(12):1228–1229.

32. Waelter S, et al. (2001) Accumulation of mutant huntingtin fragments in aggresome-like inclusion bodies as a result of insufficient protein degradation. *Molecular biology of the cell* 12(5):1393–407.

33. Li, X, et al. (2010) Inhibiting the ubiquitin-proteasome system leads to preferential accumulation of toxic N-terminal mutant huntingtin fragments. *Human molecular genetics*. (19): 2445–2455

34. Juenemann K, et al. (2013) Expanded polyglutamine-containing N-terminal huntingtin fragments are entirely degraded by mammalian proteasomes. *Journal of Biological Chemistry* (288): 27068–27084.

35. Hoffner G, Djian P (2014) Monomeric, oligomeric and polymeric proteins in huntington disease and other diseases of polyglutamine expansion. *Brain Sciences* 4(1):91–122.

36. Lajoie P, Snapp EL (2010) Formation and toxicity of soluble polyglutamine oligomers in living cells. *PLoS ONE* 5(12).0015245.

37. Leitman J, Ulrich Hartl F, Lederkremer GZ (2013) Soluble forms of polyQ-expanded huntingtin rather than large aggregates cause endoplasmic reticulum stress. *Nature Communications* 4:1–10.

38. Sathasivam K, et al. (2009) Identical oligomeric and fibrillar structures captured from the brains of R6/2 and knock-in mouse models of Huntington's disease. *Human Molecular Genetics* 19(1):65–78.

39. Sathasivam K, et al. (2001) Centrosome disorganization in fibroblast cultures derived from R6/2 Huntington's disease (HD) transgenic mice and HD patients. *Human molecular genetics* 10(21):2425–2435.

40. Ströhl F, Kaminski CF (2015) A joint Richardson—Lucy deconvolution algorithm for the reconstruction of multifocal structured illumination microscopy data. *Methods and Applications in Fluorescence* 3(1):14002.

Figure 1. Perinuclear aggresomes sequester and deplete soluble HDQ72 from the cytosol.

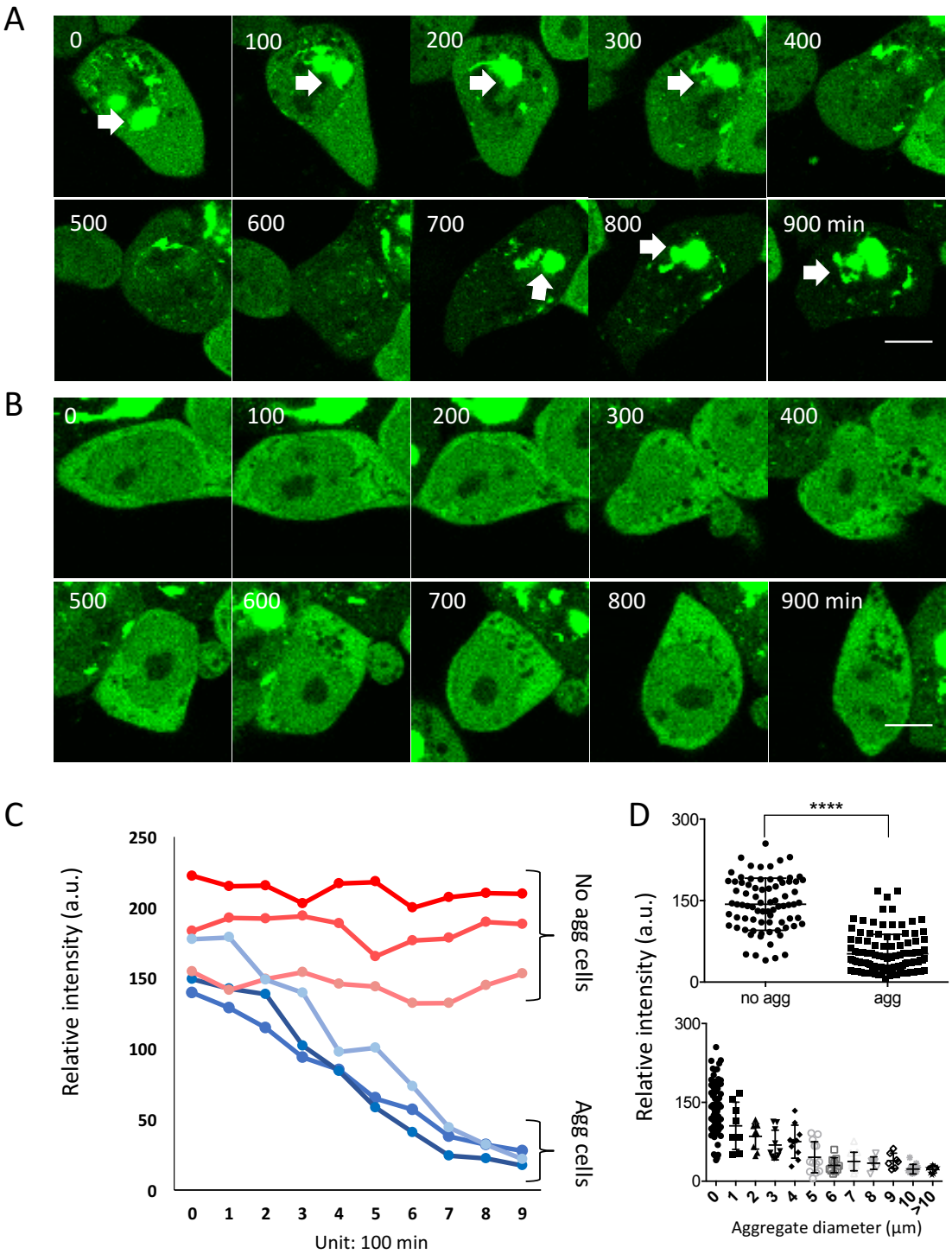

Figure 2. PolyQ aggregates undergo frequent fusion and fragmentation events in the cell.

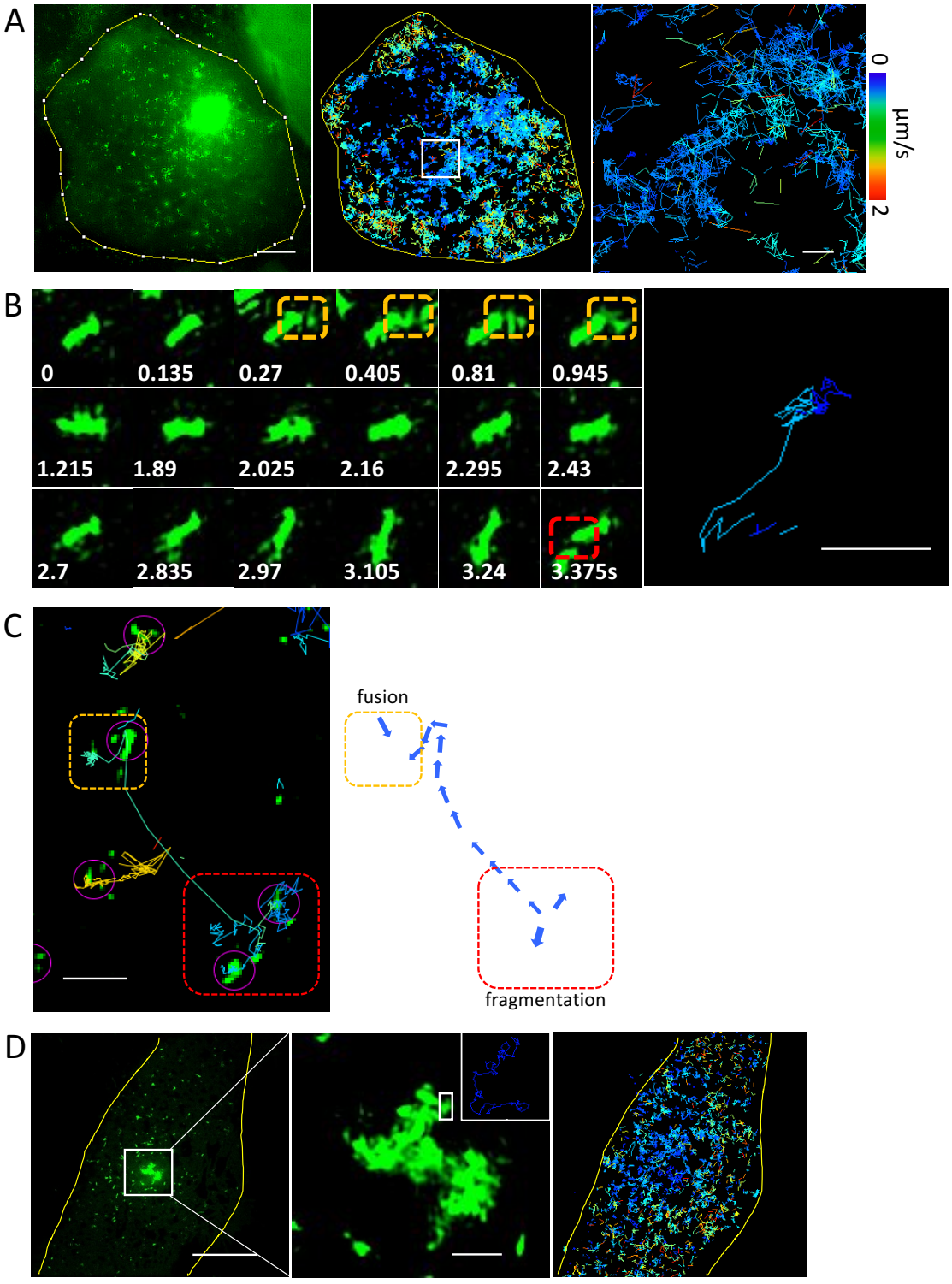

Figure 3. Most of polyQ aggregates do not colocalise with HDAC6 nor microtubules.

A

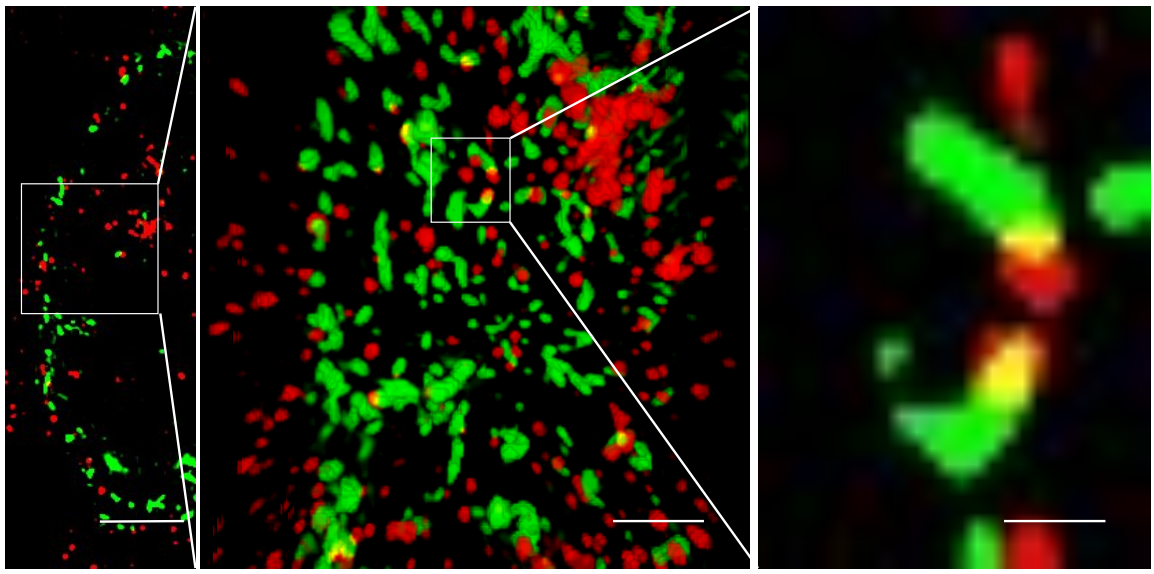

B

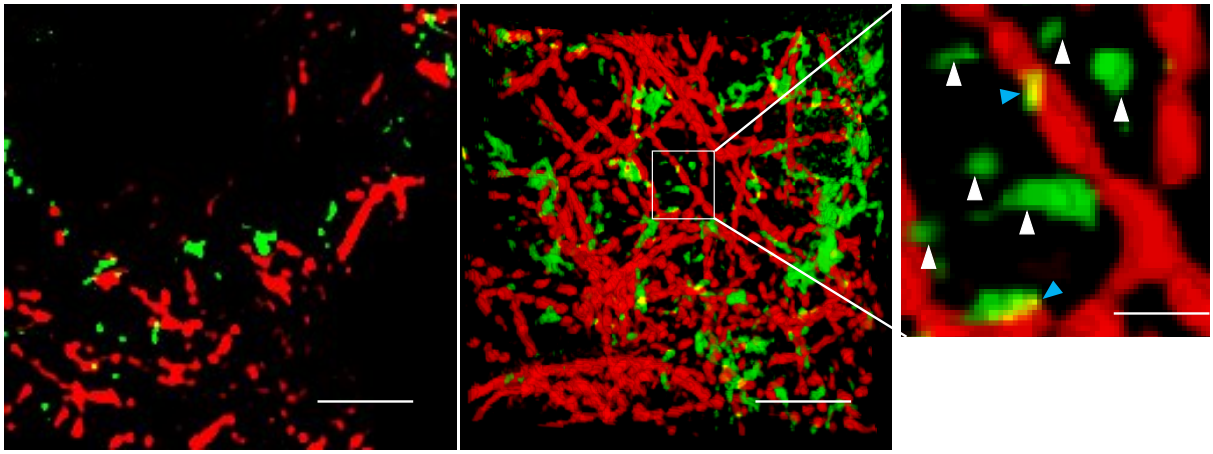

Figure 4. High resolution optical imaging of intracellular HDQ72-SNAP aggresome morphology.

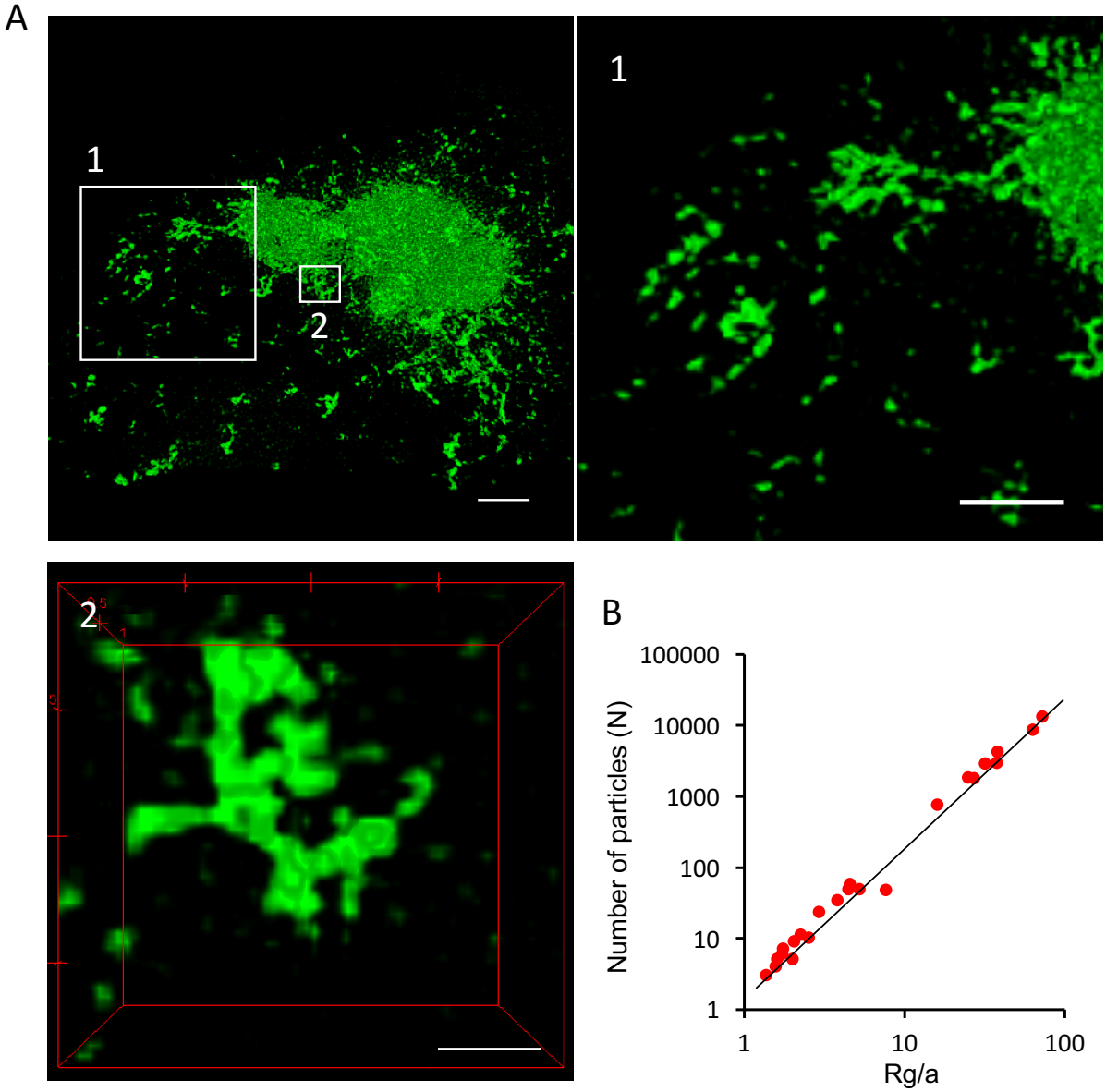

Figure 5. *in silico* modelling of aggresome formation

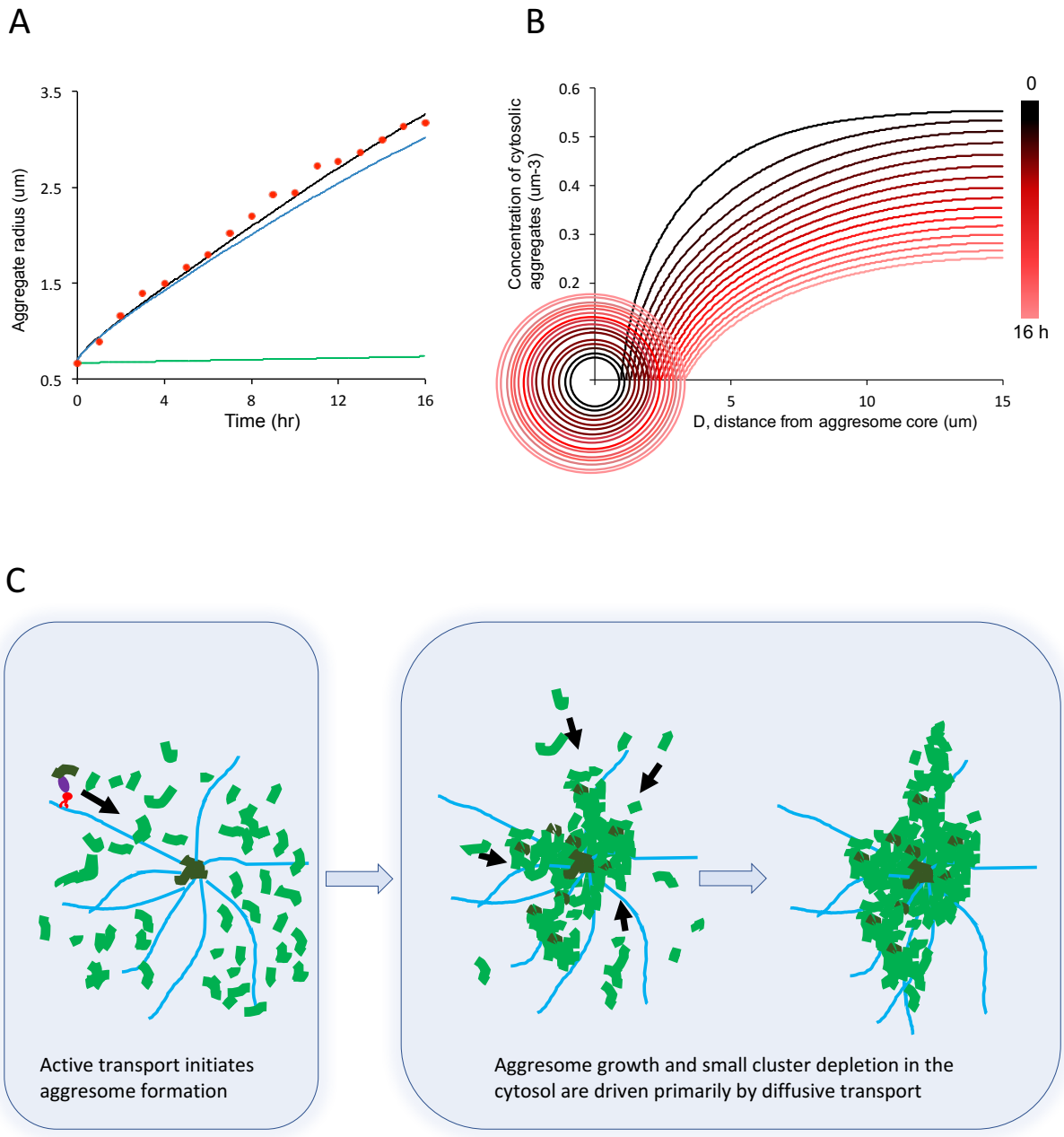

Figure 6. Dynamic imaging of aggresome growth.

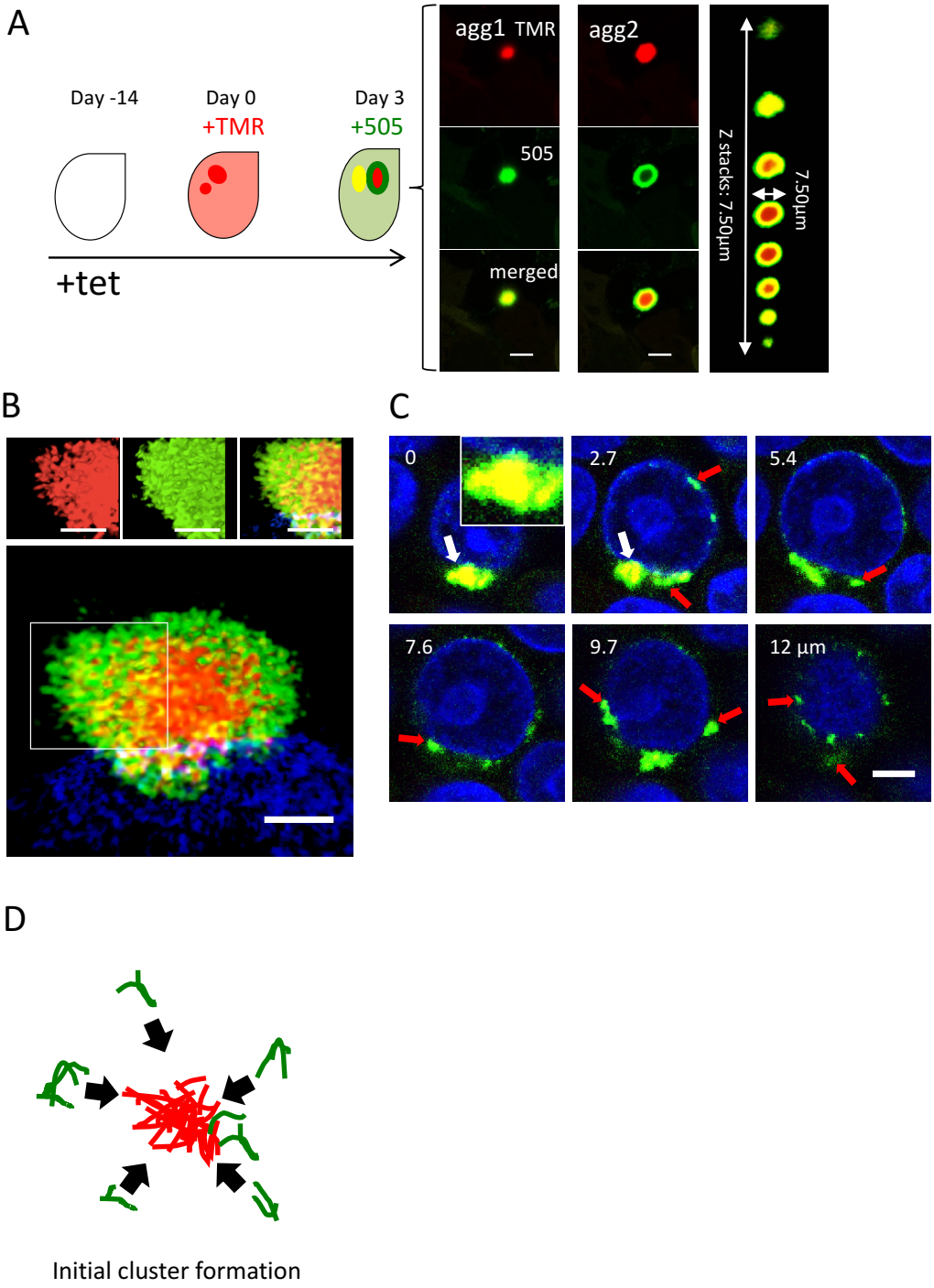

Figure 7. Intranuclear aggregates in HEK cells have a similar morphology to those observed in an R6/2 mouse model.

A Cell models

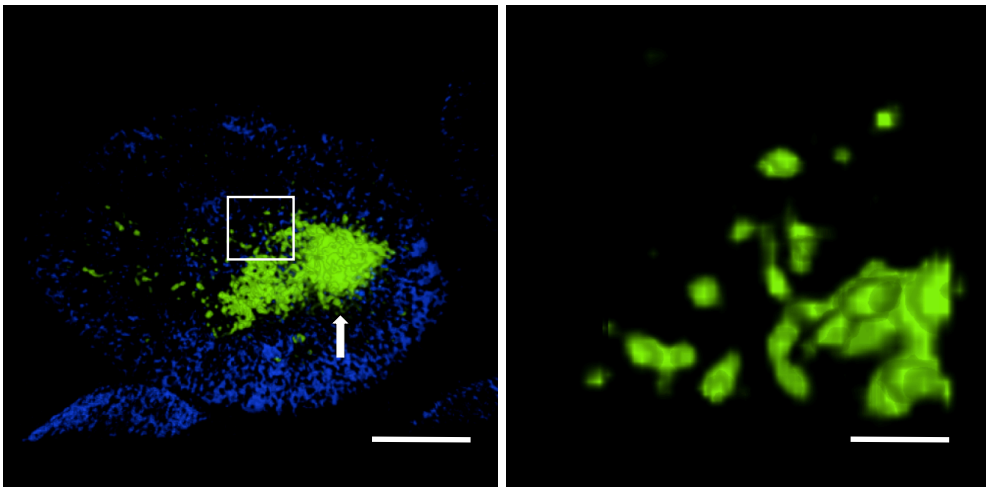

B Mouse model

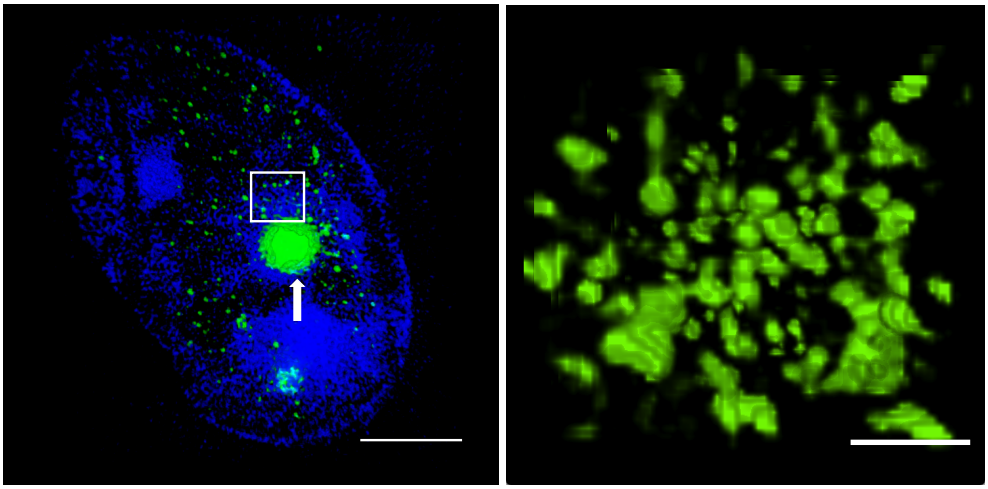

Figure S1

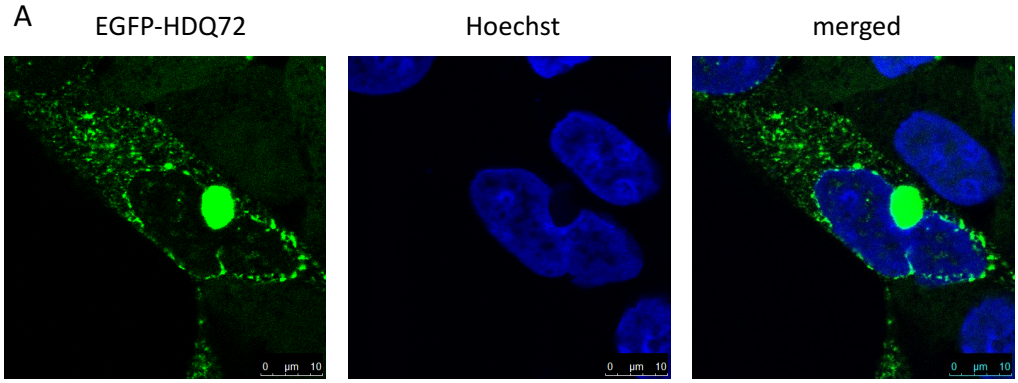

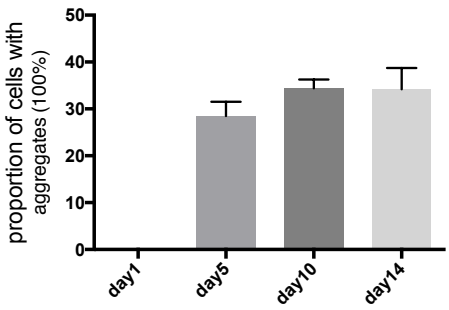

Figure S2

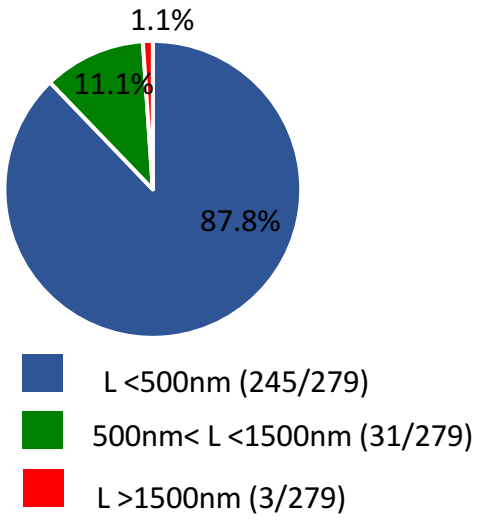

Figure S3

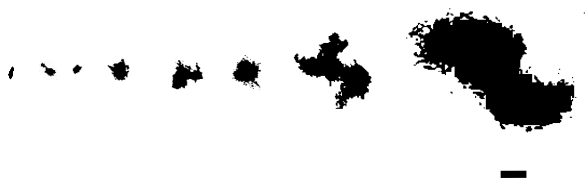

Figure Legends

Figure 1. Perinuclear aggresomes sequester and deplete soluble HDQ72 from the cytosol.

(***A***) Time-lapse images recorded by confocal microscopy of an aggregate-containing cell over a time period of 15 h. The cytoplasmic concentration of soluble EGFP-HDQ72 protein is seen to decrease over time, as it is subsumed into the large perinuclear aggresome. White arrows highlight a perinuclear aggresome. Scale bar: 10 μm.
(***B***) Time-lapse images of a cell in which no aggregation takes place over a period of 15 h. There is no noticeable decrease of the cytosolic fluorescence signal, indicating that the concentration of EGFP-HDQ72 remains constant. Scale bar: 10 μm.
(***C***) Plot of the fluorescence intensity change for recordings such as shown in ***A***) and ***B***). Results are shown for three cell samples containing aggresomes (blue colours) and three which were devoid of aggresomes (red colours).
(***D***) Upper panel: Average fluorescence intensity from the cytosol of aggresome-free (N=78) and aggresome-containing (N=106) cells. Error bars correspond to standard deviations from the mean. **** indicates a P value<0.0001 in an unpaired *t*-test. Lower panel: Correlation of average cytoplasmic fluorescence intensity with the size of perinuclear aggresomes observed (N=106).

Figure 2. PolyQ aggregates undergo frequent fusion and fragmentation events in the cell.
(***A***) High-speed SIM recordings of intracellular aggregate dynamics. All small aggregates are subjected to dramatic random movements, which lead to collisions and contacts among clusters. Using a SPT algorithm we identified individual particles and analysed their trajectories in time at a frame rate of 5 Hz (middle and right-hand panel). The velocity spectrum shown applies to all panels. Scale bars: 5 μm (left panel), 1 μm (right panel).
(***B***) Example images of individual particles in quasi-random motion. Dashed orange and red rectangles highlight fusion and fission events, respectively. Scale bars: 500 nm.
(***C***) Aggregate motion includes both active and passive transport components. The purple circles highlight regions where small clusters where identified in the automated analysis. The dashed orange and red rectangles indicate regions where fusion and fragmentation take place, respectively. Scale bar: 2 μm.
(***D***) Loose clusters in the periphery of the aggresome are highly mobile. The panels show motion paths of individual fragments within the aggresome (middle panel). SPT reveals that the mobility of

aggregate fragments is higher in the in the cytosol than in the aggresome (right hand panel). Scale bars: 5 μm (left panel), 1 μm (middle panel).

Figure 3. Most polyQ aggregates do not colocalise with HDAC6 nor microtubules.

(***A***) Left: A section slice of cytosolic aggregates (green) in HEK cells that are immunostained against HDAC6 (red) and α-tubulin (green). Middle: Magnified 3D rendering of the marked region from left. Right: Magnified 3D rendering of the marked region from middle panel, showing examples of small polyQ clusters bound to HDAC6, which represents a very small proportion of the total. Scale bars from left to right: 4 μm, 1 μm and 300 nm, respectively.

(***B***) left: A section slice of cytosolic aggregates (green) in HEK cells that are immunostained against α-tubulin (red). Middle: 3D rendering of the region from left. Right: Magnified rendering of the marked region from middle, showing examples of small polyQ clusters either bound to microtubules (blue arrowheads), in which the yellow colour indicates the colocalisation of the two parts, or dissociated from microtubules (white arrowheads). Scale bars from left to right: 2 μm, 2 μm and 400 nm, respectively.

Figure 4. High resolution optical imaging of the morphology of an intracellular HDQ72-SNAP aggresome.

(***A***) High resolution SIM images of an aggresome and its peripheral regions. The highlighted regions (1-2) are shown in the corresponding panels. Scale bars: 2 μm. 1) Zoomed in view of peripheral region of the aggresome containing individual, unconnected aggregate fragments that are not associated with the main body of the aggresome. 2) Example of amorphous small protrusions from the aggresome surface, containing fused aggregate fragments that have arrived from the cytosol. Scale bars: 1 μm (1) and 500 nm (2).

(***B***) Number of particles in an aggregate N as a function of cluster radius of gyration R_g for all aggregate clusters, where we can derive the fractal dimension D_f. a refers to the radius of the elementary building block made up of small aggregate clusters which, for modelling purposes, is assumed to be spherical.

Figure 5. Mathematical modeling of aggresome formation

(***A***) Modeling of two modes of assembly pathways in aggresome formation. Aggresome formation driven by diffusion (blue line) is a closer fit to the real experimental data shown in red spots, indicating a greater contribution to aggresome expansion. Green line represents pure MT dependent active transport. The black line represents the combined modes of diffusion and active transport.

(***B***) Modeling of aggresome expansion with decreasing cytosolic aggregate concentration. Each line represents the size of aggresome and cytosolic aggregate concentration; the null concentration point of each line represents the interface of aggresome and cytosol, whose value on the *x*-axis shows the aggresome radius that increases in time. The circles represent the expanding aggresome at different time points in this modelling.

(***C***) Schematic of the process of aggresome formation. Expression of aggregation-prone protein HDQ72 leads to accumulation of aggregate clusters in cytosol. These clusters can be recruited by HDAC6 and undergo MT-dependent active transport or diffusion. Aggregate clusters undergoing active transport are delivered to the MTOC and form a nucleation core on which other aggregate clusters can assemble. As aggresomes expand in size, it provides a greater surface area to interact with diffusing aggregates, thus recruiting them at a faster rate and accelerating aggresome growth. Therefore, aggresome expansion driven by diffusion is an irreversible process that depletes the cytosol of HDQ72. MTs are shown in light blue, cytosolic aggregate clusters undergoing diffusion are in green, aggregate clusters undergoing active transport are in dark green, HDAC6 is in purple and dynein in red.

Figure 6. Dynamic imaging of aggresome growth.

(***A***) - (***C***) The aggresome core becomes increasingly dense and impermeable over time.

(***A***) Cartoon to demonstrate the two-colour labelling protocol. Cells expressing SNAP-HDQ72 were labelled with TMR-Star at day 0 (red colour), and three days later with 505-Star (green). Confocal images reveal two types of aggresome. In early-stage aggresomes, newly added material diffuses into core domains, leading to complete overlap of the two colours in the images. In contrast, late-stage aggresomes become increasingly impermeable (dense) and the newly adsorbed material remains spatially distinct from the core region. Scale bar: 5 μm. Right panel: confocal slices for agg2.

(***B***) 3D SIM images of an impermeable aggresome. Labelling protocol as in (***A***). Both the inner part and peripheral regions of aggregates were composed of small clusters. Scale bar: 2 μm.

(***C***) Sequential labelling with alternating dyes reveals that the core region becomes increasingly impermeable over time. Scale bar: 7.5 μm.

(***D***) Cartoon to illustrate aggresome formation. Multiple fragments (green) cluster around a central seeding site (red) to form a large aggregate core.

Figure 7. Intranuclear aggregates in HEK cells have a similar morphology to those observed in an R6/2 mouse model.

(***A***) 3D SIM images of intranuclear aggregates in the HEK cell model expressing SNAP-HDQ72. Numerous small clusters and a large aggregate were embedded inside nucleus. The right-hand panel shows a zoomed-in version of the region in the white rectangle. Scale bars: 2 μm (left panel), 500 nm (right panel).
(***B***) 3D SIM images of immunostained intranuclear polyQ aggregates in the R6/2 mouse model at 14 weeks of age. The aggregates feature a similar morphology to that observed in the cell model. Right panel: zoomed-in region shows the amorphous clusters. Scale bars: 2 μm (left panel), 500 nm (right panel).

Supporting Information

1. Mathematical model of aggresome growth

To support and better understand the experimental observations, a mathematical model has been developed to describe the formation and growth Poly-Q perinuclear aggresome.

The system will be modelled as composed of a spherical aggresome, considered to be a fractal aggregate with well-defined radius of gyration and made of elementary building blocks (clusters) all with the same average size and an effective diffusion coefficient. The aggresome is located at the centre of a cell supposed to be a perfect sphere. The space between the aggresome and the cell boundary is filled with cytosol. The cytosol is populated homogeneously by clusters taken to be spherical objects characterized by the same size, so the presence of any poly-Q monomer in the liquid medium is neglected.

Considering the geometry of the system, a spherical symmetry condition has been hypothesized, so that the concentration of Poly-Q in the liquid phase, expressed as $clusters/m^3$, will depend on time and radial coordinate only. The model describes the growth of only one large aggresome at the center of the cell, neglecting the formation of other Poly-Q agglomerates.

As it was mentioned earlier, the transport of the clusters from the cytosol to the aggresome is governed by two different effects, Brownian motion along the radial direction and active transport through a MTs. These two contributions will be considered to be independent from one other, so when a cluster will enter the MTOC it won't be influenced by the diffusive transport that takes place inside the cytosol. Finally, it has been evaluated the initial concentration of clusters inside the cell thanks to image analysis. Great attention was paid to this step: as mentioned earlier, only 5% of the total clusters are

under active transport and this proportion will be considered during the initialization of the input parameters.

The model thus reduces to a moving-boundary Stefan problem where two distinct transport processes take place at the same time. This leads to two separate Cauchy problems, for diffusive and active transport, respectively, in a spherical geometry with a moving-boundary given by the interface between solid aggresome (growing as a function of time) and the liquid-like cytosol which fills the surrounding space. Conservation of matter at the solid-liquid (or aggresome-liquid interface) interface is implemented to describe the quantity of Poly-Q migrating into the growing aggresome and to update the position of the radius of the increasing aggresome (the moving lower boundary of the domain where the differential equations are solved).

The two Cauchy problems have been formulated for diffusive and active transport and are shown below in equation (1)-(7): every building-block (cluster) is either moving under Brownian motion in the cytosol or being actively transport (advected) inside one of the MTOC. For the diffusive transport we have the following diffusion equation with its boundary and initial conditions:

$$\partial_t C^B_{liq} = D\partial^2_r C^B_{liq} + \frac{2D}{r}\partial_r C^B_{liq} \qquad R < r < R_{cell} \tag{1}$$

$$C^B_{liq}(r,t) = 0 \qquad r = R \tag{2}$$

$$\partial_r C^B_{liq}(r,t) = 0 \qquad r = R_{cell} \tag{3}$$

$$C^B_{liq}(r,t) = C^B_{liq,0} \qquad t = 0 \tag{4}$$

while for the advective transport in the MTOC we have the following pure-advection equation with its boundary conditions:

$$\partial_t C^C_{liq} = -V_r \partial_r C^C_{liq} \qquad R < r < Rcell \tag{5}$$

$$\partial_r C^C_{liq}(r,t) = 0 \qquad r = R_{cell} \tag{6}$$

$$C^C_{liq}(r,t) = C^C_{liq,0} \qquad t = 0 \tag{7}$$

D is the diffusion coefficient, considered to be constant along the radial coordinate, V_r is the radial component of the advection speed inside the MTOC (taken to be independent of r, based on experimental evidence), R the radius of the growing aggresome corresponding to the position of the solid-liquid interface during time, R_{cell} the characteristic size of the cell taken to be spherical, $C^B_{liq,0}$ the initial concentration of clusters inside the cytosol that will be transported by Brownian motion, and $C^C_{liq,0}$ is the initial concentration of clusters inside the MTOC that are subsequently transported by pure advection to the aggresome.

The update of the solid-liquid interface is obtained by enforcing conservation of matter at the aggresome interface $r = R$: the RHS of equation (8) below represents the flux of matter that is included in the solid phase during the time span δt. This leads to the deposition of an external shell of aggregates to the surface of the aggresome that causes an increase of the mass of the aggresome expressed in the LHS of (8).

$$q\frac{4}{3}\pi(R(t+\delta t)^3 - R(t)^3) = 4\pi \int_t^{t+\delta t} R(\tau)^2 \left[\left(\partial_r C^B_{liq}(R(\tau),\tau)\right) - V_r C^C_{liq}(R(\tau),\tau)\right] d\tau \tag{8}$$

In this case τ represents the temporal variable integrated between t and $t + \delta t$, meanwhile q represents the amount of matter necessary to increase the system by a unit of volume. Because the aggresome is a fractal aggregate, its density (number of building blocks per unit volume) is not constant, and decreases over time because of the spatially self-similar nature of the growth process. It is possible to relate $q(t)$ to the fractal dimension d_f of the aggresome and its radius of gyration R, and to the radius of the single building block (cluster) a via the following relation

$$q(t) = \frac{k_g (R(t)/a)^{d_f - 3}}{\frac{4}{3}\pi a^3} \tag{9}$$

The fractal scaling prefactor k_g and the fractal dimension d_f are related to the number of building blocks N inside the aggresome via the standard fractal scaling relation

$$N = k_g \left(R(t)/a\right)^{d_f} . \tag{10}$$

Even though q varies with time overall, it will be considered constant over the small time-step δt taken for the discretization of the transport equations. Dividing both intervals by δt and doing the limit for $\delta t \rightarrow 0$ we obtain

$$\lim_{\partial t \to 0} \frac{4\pi q}{3} \frac{R(t+\delta t)^3 - R(t)^3}{\delta t} = \lim_{\delta t \to 0} \frac{4\pi}{\delta t} \int_t^{t+\delta t} R(\tau)^2 \left[\left(\partial_r C_{liq}^B (R(\tau), \tau) \right) - V_r C_{liq}^C (R(\tau), \tau) \right] d\tau \tag{11}$$

Because the integrand function in (11) is continuous and limited inside every interval $[t,t+\delta t]$ it is possible to apply the Mean Value Theorem (MVT) defined in (12)

$$\frac{\int_t^{t+\delta t} R(\tau)^2 \left[\left(\partial_r C_{liq}^B (R(\tau), \tau) \right) - V_r C_{liq}^C (R(\tau), \tau) \right] d\tau}{\delta t} = \tag{12}$$
$$= R(t_{int})^2 \left[\left(\partial_r C_{liq}^B (R(t_{int}), t_{int}) \right) - V_r C_{liq}^C (R(t_{int}), t_{int}) \right]$$

where t_{int} is an intermediate point inside the interval $[t,t + \delta t]$. Applying MVT together with the definition of the first derivative IN (11) we obtain

$$\frac{4\pi q}{3} \partial_t [R(t)^3] = \lim_{\delta t \to 0} 4\pi R(t_{int})^2 [\left(\partial_r C_{liq}^B (R(t_{int}), t_{int}) \right) + \tag{13}$$
$$- V_r C_{liq}^C (R(t_{int}), t_{int})].$$

Finally (13) can be reduced to the following final equation through some simple mathematical passages

$$\partial_t R(t) = \frac{D}{q} \partial_r C_{liq}^D (R(t), t) - \frac{V_r}{q} C_{liq}^C (R(t), t) \qquad t > 0 \tag{14}$$
$$R = R_0 \qquad t = 0. \tag{15}$$

Equation (13) is numerically solved with an explicit first order finite difference scheme where q will be maintained constant over each time span and equal to its value related to the lower limit of every

interval; of course a proper time step needs to be chosen such that the approximation of q being constant over each time interval will lead to reliable results.

Full details about the numerical resolution of the model and the input data adopted are provided in the supporting information.

2. Numerical solution

The system (1)-(4) can be numerically solved by using the Crank-Nicholson method: the continuous space coordinate will be divided into a series of N discrete intervals and the implicit finite difference scheme will be applied for $j = n+1,..,N$ where $n+1$ is the node related to the solid-liquid interface; (16) is a general line of the linear system that needs to be solved.

$$A(j)C_{j+1}^{i+1} + (1+B)C_j^{i+1} - E(j)C_{j-1}^{i+1} = A(j)C_{j+1}^{i} + (1-B)C_j^{i} + E(j)C_{j-1}^{i} \quad (16)$$

The values of the coefficients A(j), B and E(j) are reported in (17) - (19)

$$A(j) = \left(\frac{D\delta t}{2\delta r^2} + \frac{D\delta t}{2r_j\delta r}\right) \quad (17)$$

$$B = \frac{D\delta t}{\delta r^2} \quad (18)$$

$$E(j) = \left(\frac{D\delta t}{2\delta r^2} - \frac{D\delta t}{2r_j\delta r}\right) \quad (19)$$

δr is the interval between two consecutive nodes and δt is the time step adopted in this work.

The two boundary conditions (2)-(3) can be respectively written as

$$C_{liq}^{D}(n+1,t) = 0 \quad (20)$$

$$C_{liq}^{D}(N-1,t) = C_{liq}^{D}(N+1,t) \quad (21)$$

The second one represents as a symmetry condition that, thanks to the use of a ghost node $N+1$: the N^{th} point of the grid can be used as a mirror between neighbouring cells; so the coefficients of the last line of the linear system become

$$A^D(N) = B^D = E^D(N) = \left(\frac{D\delta t}{\delta r^2}\right) \tag{22}$$

Regarding the other Cauchy problem, it has been demonstrated that the analytical solution of a pure convection equation, knowing the initial concentration

$D = 1.36\ 10^{-15}$	m^2/s
$V_r = -7.0\ 10^{-10}$	m/s
$R_{cell} = 1.5\ 10^{-5}$	m
$C^B_{liq,0} = 5.7\ 10^{17}$	$aggregates/m^3$
$C^C_{liq,0} = 3.0\ 10^{16}$	$aggregates/m^3$
$\delta t = 3.6$	s
$\delta r = 9.25\ 10^{-9}$	m
$R_0 = 6.67\ 10^{-7}$	m
$a = 1.95\ 10^{-7}$	m

Table 1: list of input data together with the respective SI units adopted in this work distribution

$C_{liq,}{}^{C}{}_{0}$, is

$$C^C_{liq}(r,t) = C^C_{liq,0}(r - V_r t, t) \tag{23}$$

Thanks to (22), the active transport of aggregates inside the microtubes can be modelled as a plug flow of matter from the cell liquid medium to the aggresome. In the main text we describe the theoretical

approach to update the position of the solid-liquid interface, what follows is the explicit first order discretization adopted in this work

$$R_{i+1} = R_i + \frac{D\delta t}{q_i}\frac{(C^D_{n+2,i} - C^D_{n+1,i})}{\delta r} - \frac{V_r}{q_i}(C^C_{n+1,i}) \qquad (24)$$

The evaluation of q_i at each time step can be done through equation (9), but before it has been necessary the evaluation of k_g and d_f using (10). Experimentally it was possible to find $k_g = 1.75$ and $d_f = 2.08$; finally, the complete list of input data is shown in Table 1; the value of V_r is considered as negative because the direction of the active transport is opposite as the one related to the radial direction considered in this work.

Figure S1

A. Confocal images of an EGFP-HDQ72 cell with an aggresome visible in the perinuclear area.

B. Proportion of EGFP-HDQ72 cells containing aggregates at different time points after tetracycline induction. Three independent experiments were performed with around 200 cells assessed per population per experiment.

Figure S2

Quantification of aggregate cluster numbers of different length scales. Cell samples were fixed and 279 aggregate clusters were recorded and analysed by 3D SIM.

Figure S3

Examples of binary images of aggregates used for gyration radius analysis. Scale bar: 1 μm.

Video 1. High-speed SIM recording (2 Hz) of cytosolic polyQ aggregates.

Video 2. High-speed SIM recording (6 Hz) of aggregate particles in quasi-random motion.

Video 3. High-speed SIM recording (2 Hz) of small cluster motion within an aggresome.

Video 4. 3D SIM reconstruction of an aggresome and small aggregate clusters.

Video 5. 3D SIM reconstruction of a small, amorphous cluster.